Journal of Materials Chemistry

Cite this: *J. Mater. Chem.*, 2011, **21**, 6217

www.rsc.org/materials

**PAPER**

# *In situ* electrochemical doping enhances the efficiency of polymer photovoltaic devices†

**Ming-Shin Su,[a] Hai-Ching Su,[b] Chih-Yin Kuo,[a] Yi-Ren Zhou[a] and Kung-Hwa Wei*[a]**

***Received 20th October 2010, Accepted 9th February 2011***
**DOI: 10.1039/c0jm03550e**

In this study, we found that the formation of a p–i–n junction through *in situ* electrochemical doping is a promising way to enhance the performance of polymer photovoltaic devices. We applied a pre-bias to metal triflate [LiOTf, KOTf, $Ca(OTf)_2$, $Zn(OTf)_2$]/poly(ethylene oxide) (PEO)–incorporated poly[5-(2′-ethylhexyloxy)-2-methoxy-1,4-phenylenevinylene] (MEH-PPV)/{6}-1-(3-(methoxycarbonyl) propyl)-{5}-1-phenyl-[5,6]-$C_{61}$ (PCBM) photovoltaic devices to form p–i–n junctions in their active layers. Auger depth profile analyses and alternating-current capacitance analyses of these doped devices revealed that the positive and negative ions were distributed unequally to form an asymmetrical p–i–n structure in a thin layer of *ca.* 100 nm of the polymer, and the intrinsic layer became thinner when formed under a higher pre-bias voltage. Atomic force microscopy and transmission electron microscopy revealed that the addition of metal triflate/PEO to MEH-PPV/PCBM improved the morphology of the composite films. Among the various doped devices, the MEH-PPV/PCBM device incorporating a LiOTf/PEO mixture exhibited the highest power conversion efficiency, a 40% increase relative to that of the reference device (MEH-PPV/PCBM).



## Introduction

Organic photovoltaic devices are attracting much attention because of their potential for use as cheap, large-area, flexible devices. Such devices featuring a bulk heterojunction (BHJ) structure exhibit much higher power conversion efficiencies (PCEs) than corresponding non-heterojunction devices because of their larger interfacial areas for exciton dissociation.[1–6] Much effort has been made to optimize the internal structures of polymer solar cells to increase their lifetimes and PCEs; for example, modifying the work functions of the electrodes[7,8] by incorporating metal oxides such as $TiO_x$, $MoO_3$, $WO_3$ and $V_2O_5$ between the active layers and electrodes[9,10] and taking advantage of nano-scale effects, have been carried out.[11,12] Phase compatibility and overall uniformity of the film roughness are critically important properties for the optimal performance of polymer solar cells.[13,14] Nevertheless, the built-in potential across the disordered active layer, with a thickness of *ca.* 100 nm, which is essential for efficient light absorption, leads to a relatively lower built-in electric field and thus, lower carrier collection efficiency.[15–19] These obstacles, which are also encountered in small-molecule solar cells, can be partially overcome by fabricating organic solar cells with a p–i–n architecture.[20–23] Recently, a small-organic-molecule p–i–n structure was developed by doping small-molecule organic layers to increase the conductivity and, therefore, ensure efficient charge transport and the formation of ohmic contacts at organic–metal interfaces.[24] As a result, the built-in potential is predominant and strong across the resistive and thin intrinsic regions, rendering a higher built-in electric field and, consequently, a higher carrier collection efficiency.

Polymer photovoltaic devices can be conveniently fabricated using cost-effective solution processing techniques, such as spin-coating or inkjet printing, making them attractive for large-area applications. Nevertheless, multilayered polymer p–i–n structures are not readily fabricated through solution processing because of interfacial mixing problems. One promising approach toward polymer p–i–n photovoltaic devices is the use of *in situ* electrochemical doping.[25] The active layer of such photovoltaic devices contains salts with mobile ions, which can drift towards electrodes under an applied bias. For light-emitting electrochemical cells (LECs), the spatial separation of ions that induce doping (oxidation and reduction) of the active materials near the electrodes (*i.e.*, p-type doping near the anode and n-type doping near the cathode) has been demonstrated previously.[26,27] The p–i–n structure is, therefore, formed *in situ* under bias in a single-layered thin film, which is readily fabricated through solution processing. Two types of polymer-based chemically fixed p–i–n photovoltaic devices have been prepared using such

[a]*Department of Materials Science and Engineering, National Chiao Tung University, 1001 Ta Hsueh Road, Hsinchu, 30050, Taiwan, ROC. E-mail: khwei@mail.nctu.edu.tw; Fax: +886-3-5724727; Tel: +886-3-5731771*

[b]*Institute of Lighting and Energy Photonics, National Chiao Tung University, 301 Gaofa 3rd. Road, Tainan, 71150, Taiwan, ROC*

† Electronic supplementary information (ESI) available: current density–voltage and EQE curves of p–i–n MEH-PPV/PCBM photovoltaic devices, enlarged Auger depth profile consequence. See DOI: 10.1039/c0jm03550e

*in situ* electrochemical doping.[28,29] Both exhibit improved photovoltaic device performance because of the presence of the p–i–n architecture. We believed that the PCEs of polymer p–i–n photovoltaic devices could be further improved for practical applications by optimizing the donor/acceptor systems with appropriate ions. The effect of varying the nature of the salt on the morphologies and electrical properties at different pre-bias voltages of donor/acceptor blend films has not been explored previously.

In this study, we employed electrochemical doping by applying different pre-bias voltages to poly[5-(2′-ethylhexyloxy)-2-methoxy-1,4-phenylenevinylene] (MEH-PPV)/{6}-1-(3-(methoxycarbonyl)propyl)-{5}-1-phenyl-[5,6]-$C_{61}$ (PCBM) photovoltaic devices incorporating metal triflate salts [LiOTf, KOTf, $Ca(OTf)_2$, $Zn(OTf)_2$] into poly(ethylene oxide) (PEO) to form ionic complex mixtures. We used atomic force microscopy (AFM) and transmission electron microscopy (TEM) to examine the surface roughness and the morphology of the active layers, respectively. After the p–i–n device architecture had formed under direct current (DC) biasing, the photovoltaic properties of the devices incorporating different metal triflate/PEO mixtures were tested under AM 1.5G conditions. We used capacitance–voltage analysis to deduce the change in the width of the intrinsic layer as the formation of the p–i–n junction experienced the various DC pre-biases. With a relatively unchanged built-in potential that was predominant across a thinner intrinsic layer, the built-in electric field increased upon decreasing the thickness of the intrinsic region, rendering high carrier collection efficiencies and, thus, enhanced PCEs. We also carried out Auger depth profile analysis on the active layer to elucidate the distribution of positive and negative ions in the active layer that had experienced the pre-biases, to confirm the formation of a p–i–n junction structure.

## Experimental

MEH-PPV ($M_n$: 150 000–250 000), LiOTf (purity: 99.995%), KOTf (purity: 98%), $Ca(OTf)_2$ (purity: 99.9%), $Zn(OTf)_2$ (purity: 98%), PEO ($M_v$: 600 000), and chlorobenzene (anhydrous, 99.8%, <0.005% water) were purchased from Sigma–Aldrich. PCBM (purity: 99%) was purchased from Solenne BV. All materials were used as received without further purification.

Indium tin oxide (ITO)–coated glass substrates were precleaned and treated with UV-ozone prior to use. A layer of poly(3,4-ethylenedioxythiophene):poly(styrene sulfonate) (PEDOT:PSS; Clevios PVP AI4083, H. C. Starck) was spin-coated (5000 rpm) onto the ITO glass, followed by baking at 150 °C for 15 min in ambient atmosphere. The PEDOT:PSS–coated ITO glass was then loaded in a $N_2$-filled glove box for subsequent solution processing. The active layer was spin-coated (1500 rpm) onto the PEDOT:PSS–coated ITO glass using an appropriate solution. The thickness of the active layer (*ca.* 100 nm) was measured using a profilometer. Top contacts of Al (100 nm) were deposited through thermal evaporation at a base pressure below $1 \times 10^{-6}$ torr. A MEH-PPV/PCBM (1 : 4, w/w; 20 mg) solution in chlorobenzene (1 mL) was stirred overnight at *ca.* 60 °C in a $N_2$-filled glove box prior to use. Metal triflate (2 mg for LiOTf, 2.4 mg for KOTf, 4.3 mg for $Ca(OTf)_2$ and 4.7 mg for $Zn(OTf)_2$)/PEO (8 mg) solutions in chlorobenzene (1 mL) were stirred at room temperature (*ca.* 25 °C) for several days prior to use. The mole ratio of metal triflate ($1.282 \times 10^{-5}$ mol)/$CH_2CH_2O$ unit ($1.82 \times 10^{-1}$ mol) solution is $7 \times 10^{-4}$. MEH-PPV/PCBM/metal triflate/PEO mixtures were prepared by mixing a metal triflate/PEO solution (0.075 mL) with the MEH-PPV/PCBM solution (1 mL) and stirring overnight at *ca.* 60 °C in a $N_2$-filled glove box prior to use.

For photovoltaic analysis, devices were tested under simulated AM 1.5G irradiation (100 mW $cm^{-2}$) using a Xe lamp–based Newport 66902 150 W solar simulator. A Xe lamp equipped with an AM 1.5G filter was used as the white light source; the optical power at the surface of the sample was 100 mW $cm^{-2}$. The *J–V* characteristics were measured using a Keithley 2400 source meter. The spectrum of the solar simulator was calibrated using a PV-measurement (PVM-154) mono-Si solar cell (NREL-calibrated); a Si photodiode (Hamamatsu S1133) was used to check the illumination uniformity of the exposed area.[30,31] Reported efficiencies are the averages obtained from four devices prepared on each substrate. External quantum efficiencies (EQEs) were measured using the Optosolar SPF50 spectrum response.[32] The morphologies of the films of the active layers, which were fabricated through the same processes used for the devices, were recorded using an atomic force microscope (Digital Instruments Nanoscope IIIa) operated at a scan rate of 1.0 Hz in the tapping mode. The AC capacitance analysis was measured by Keithley 4200. The Auger depth profile analysis was studied by Microlab Auger electron microprobe (VG Scientific, UK). At the Auger depth profile etching process, we used Ar gas as the ion gun to etch the device surface and the etching area was 4 $mm^2$. Transmission electron microscopy (TEM) images were recorded using an FEI Tecnai G2 instrument operated at 120 keV. The TEM samples were first prepared using the same processing steps for preparing the devices; a sandwiched structure consisting of an active layer between two electrodes. Then, this structure was subject to a pre-bias of 3 V for 180 s prior to being immersed into a solution that consisted of 3 vol% detergent (Merck MA-03) in DI water for the electrodes exfoliation. Subsequently, we transferred the active layer that has been floating on the solution to a copper foil and submerged it in DI water for 10 s prior to vacuuming for 6 h before entering the TEM.

## Results and discussion

Fig. 1a presents the molecular structures of MEH-PPV and PCBM, which we used as donor and acceptor materials, respectively, for the active layers. The metal triflate salts [LiOTf, KOTf, $Ca(OTf)_2$, $Zn(OTf)_2$] were added in the active layers to provide mobile ions. The presence of an ion-conducting polymer, PEO, served as a solid-state solvent in blend films for undergoing salts dissociation, and also attained the ionic mobility. Fig. 1b provides a schematic representation of the operating principle of using *in situ* electrochemical doping to form p–i–n junctions in polymer photovoltaic devices. After a bias is applied, the mobile ions in the active layer drift toward the corresponding electrodes. Typically, the resultant n-type doped region would be smaller than that of p-type doped region[18,19] as indicated in a conducting atomic force microscopy (AFM) study. Fig. 1b also displays the spatially separated ions inducing doping (oxidation or reduction) of the active materials near the electrodes—p-type doping near

 

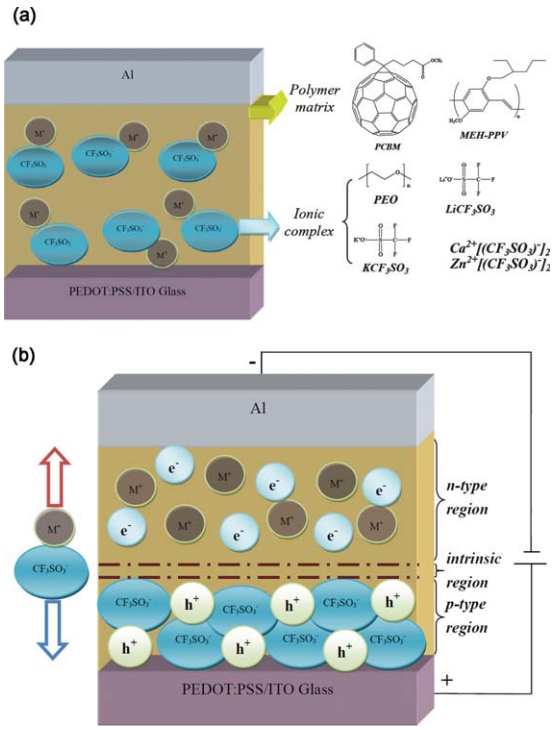


**Fig. 1** a) Device structures and molecular structures of the materials used in this study. b) Operating principle of using *in situ* electrochemical doping to form p–i–n junctions in polymer photovoltaic devices. The doping area width was a relative viewpoint and not the real width of the ion distribution.

the anode and n-type doping near the cathode. The doped regions induce ohmic contacts between the active layer and the electrodes and, consequently, reduce the voltage drop at the polymer–metal interface—a phenomenon that is beneficial for retaining the open-circuit voltage. As compared to the p- and n-type doped layers, the relatively neutral thin region—the intrinsic layer—exhibits higher resistance and, thus, the built-in potential is predominantly across this layer. Under fixed built-in potential, the built-in electric field in a thinner intrinsic layer can dissociate photogenerated excitons more effectively.[25]

To explore the phase compatibility, as well as overall uniformity, of MEH-PPV/PCBM blend films containing metal triflate/PEO mixtures, we used AFM to examine the surface morphologies of these films. Fig. 2 presents AFM images of MEH-PPV/PCBM blend films formed in the absence and presence of metal triflate/PEO mixtures. The MEH-PPV/PCBM films formed in the presence of metal triflate/PEO mixtures exhibited a much smaller root-mean-square (RMS) roughnesses (*ca.* 0.5–0.6 nm) than those of the MEH-PPV/PCBM films formed in the absence of metal triflate/PEO mixtures, indicating that addition of metal triflate/PEO mixtures into the MEH-PPV/PCBM blend films may have suppressed the phase separation of MEH-PPV and PCBM. Similar phenomena have been observed in MEH-PPV/$C_{60}$ blend films containing LiOTf/PEO mixtures.[33] Therefore, we suspected that the morphological manipulation caused by the additives might help to optimize the device performance. The transmission electron microscopy studies on these blend films provides the internal structure and morphology of them.

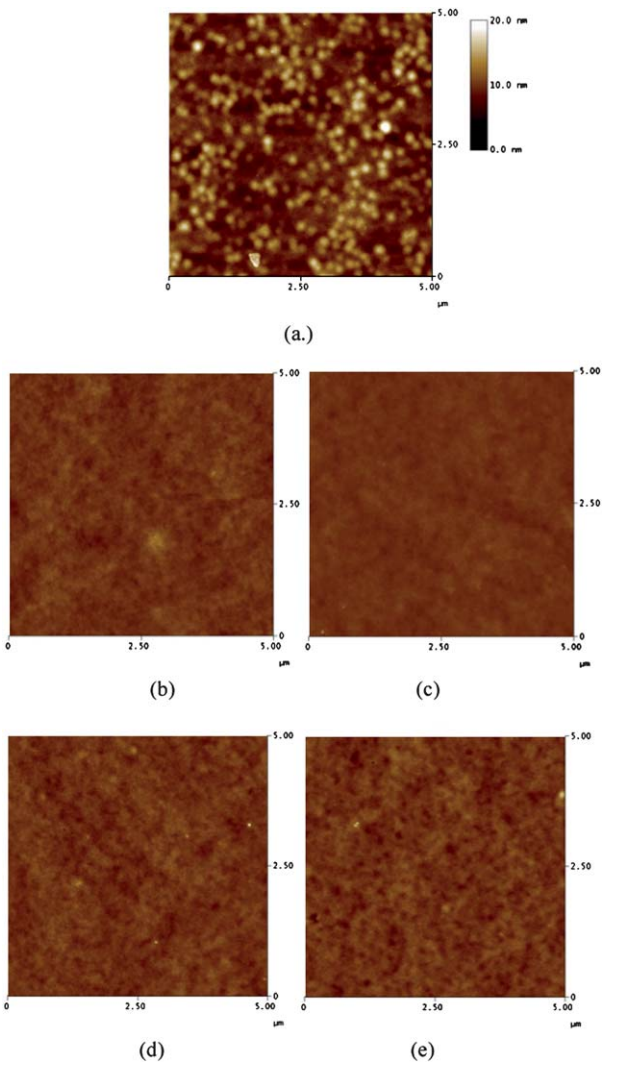


**Fig. 2** AFM images of blend films: a) MEH-PPV/PCBM (RMS = 2.003 nm), b) MEH-PPV/PCBM with LiOTf/PEO (RMS = 0.510 nm), c) MEH-PPV/PCBM with KOTf/PEO (RMS = 0.510 nm), d) MEH-PPV/PCBM with $Ca(OTf)_2$/PEO (RMS = 0.645 nm), and e) MEH-PPV/PCBM with $Zn(OTf)_2$/PEO (RMS = 0.568 nm). Area of each image: 5 μm × 5 μm.

Fig. 3 displays the TEM images of the MEH-PPV/PCBM and MEH-PPV/PCBM films incorporating LiOTf, KOTf, $Ca(OTf)_2$, or $Zn(OTf)_2$/PEO mixtures with or without applied pre-bias of 3 V for 180 s. In Fig. 3a, the bright and the dark regions can be identified as the polymer rich and the PCBM rich areas, respectively, because of the large electron density difference. In Fig. 3 b1–e1, the TEM images of the MEH-PPV/PCBM film incorporating LiOTf, KOTf, $Ca(OTf)_2$, or $Zn(OTf)_2$/PEO mixtures shows much smaller bright and dark domains than that of the MEH-PPV/PCBM film, indicating that the incorporation of the metal triflate/PEO makes the dispersion of MEH-PPV and PCBM more uniform. This compatibilizing effect is possibly due to the interaction of charged ions between MEH-PPV and PCBM. Fig. 3 b2–e2 present the TEM images of MEH-PPV/PCBM incorporating LiOTf, KOTf, $Ca(OTf)_2$, and $Zn(OTf)_2$/PEO mixtures with pre-bias of 3 V for 180 s; we can see that the

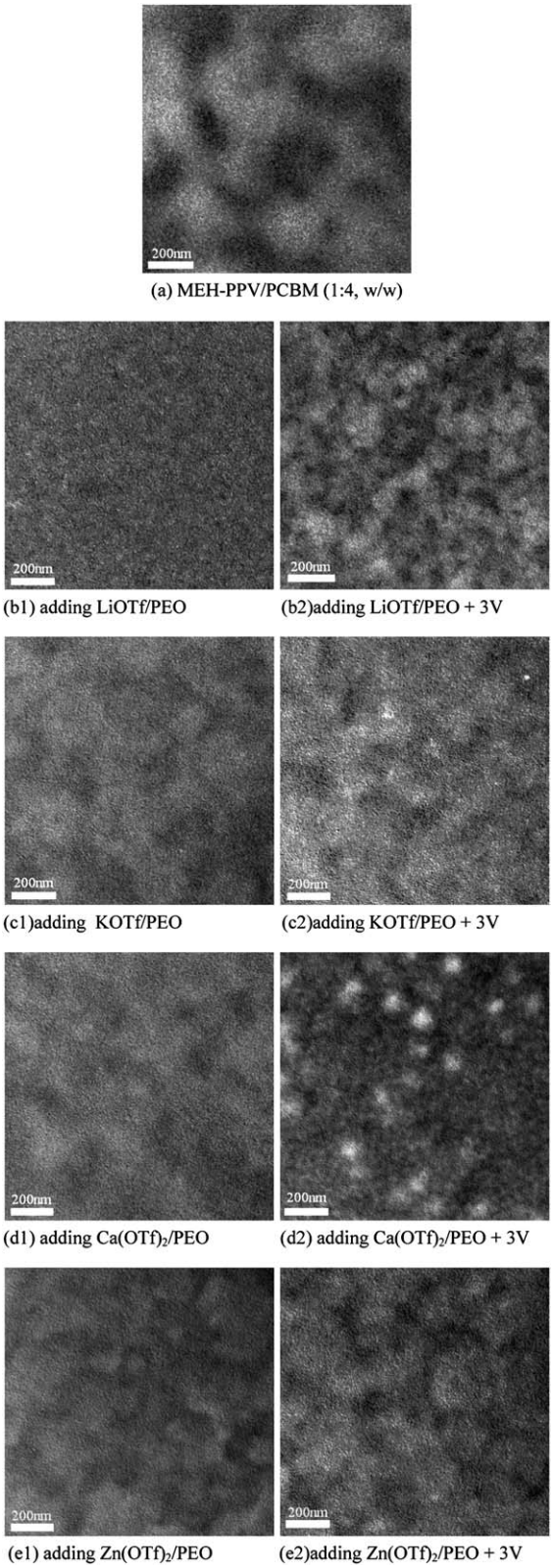


**Fig. 3** TEM images of the MEH-PPV/PCBM and MEH-PPV/PCBM films incorporating LiOTf, KOTf, $Ca(OTf)_2$, and $Zn(OTf)_2$/PEO mixtures with or without applied pre-bias of 3 V for 180 s. (a) represents the MEH-PPV/PCBM device, and (b1–e1) represent the devices of MEH-PPV/PCBM incorporating LiOTf, KOTf, $Ca(OTf)_2$, and $Zn(OTf)_2$/PEO mixtures. (b2–e2) represent the devices of MEH-PPV/PCBM incorporating LiOTf, KOTf, $Ca(OTf)_2$, and $Zn(OTf)_2$/PEO mixtures with a prebias of 3 V for 180 s.

morphology changed after experiencing the pre-bias, and the bright and dark domains become larger for any of the four types of p–i–n junction devices, implying that the applied pre-bias would not only alter the ion distribution but also change the active layer's morphology.

To clarify the mechanism for the formation of the p–i–n junctions through *in situ* electrochemical doping, we performed alternating current (AC) capacitance analyses[34,35] of the photovoltaic devices. Fig. 4 displays the capacitance of the MEH-PPV/PCBM device formed in the absence of a metal triflate/PEO mixture, measured under zero bias, as the reference. When incorporating LiOTf/PEO mixtures and applying different pre-biases for 180 s, the devices exhibit enhanced capacitance over the entire frequency range from 0.1 to 500 kHz because the ionic doping induced an increase in the dielectric constant of the active layer. Furthermore, the capacitance of the device increased upon increasing the pre-bias voltage up to 5 V. We observed similar trends for the MEH-PPV/PCBM devices incorporating the KOTf, $Ca(OTf)_2$, and $Zn(OTf)_2$/PEO mixtures. The capacitance of the MEH-PPV/PCBM devices incorporating the LiOTf/PEO mixtures that had experienced pre-biasing at 3 V for 180 s were enhanced by 10–22% relative to that of the device that had not been subjected to pre-biasing, in the frequency range from 0.1 to 500 kHz. These results are reminiscent of those obtained from AC impedance analyses of polymer LECs composed of MEH-PPV and LiOTf/PEO mixtures that had experienced a 3 V bias.[34] The increase in the capacitance can be attributed to the formation of the p–i–n junction, where the highly conductive positive ion (n-type)-doped region and negative ion (p-type)-doped region function as electrodes for the insulating intrinsic (i) region in between.[34] This phenomenon can be quantified; the capacitance of a parallel plate capacitor with area $A$, dielectric constant $\varepsilon$, and thickness $d$ can be described using equation (1):

$$C = \varepsilon \frac{A}{d} \quad (1)$$

*In situ* electrochemical doping reduces the thickness ($d$) of the relatively insulating intrinsic layer and, therefore, enhances the capacitance. A higher pre-bias voltage would result in more accumulated ions in the active layer, thereby broadening the doped regions and leading to a thinner intrinsic layer, rendering a higher capacitance. These results imply an enhanced built-in electric field in the p–i–n MEH-PPV/PCBM photovoltaic devices because the built-in potential is positioned across a thinner intrinsic layer.

In order to directly confirm the formation of the p–i–n junction structure, we performed Auger depth profile analysis on the device consisting of KOTf/PEO incorporated MEH-PPV/PCBM active layer, for detecting the ion distribution. The device structure used in Auger depth profile analysis consists of Al as the top layer, MEH-PPV/PCBM incorporating KOTf/PEO as the active layer and ITO as the bottom layer. The reason that the device studied was without a PEDOT:PSS layer is that we do not want the sulfur energy signal peak contributed to by the PEDOT:PSS layer to interfere with that contributed to by the

 

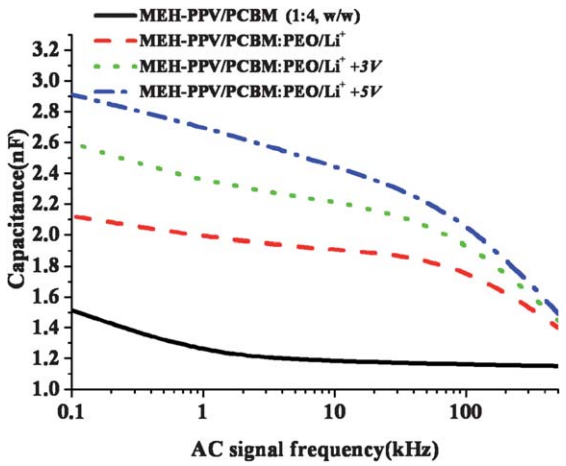


**Fig. 4** AC capacitance analysis, under zero DC biasing, at frequencies of 0.1–500 kHz, for p–i–n photovoltaic devices incorporating the LiOTf/PEO mixture that had been subjected to various pre-bias voltages.

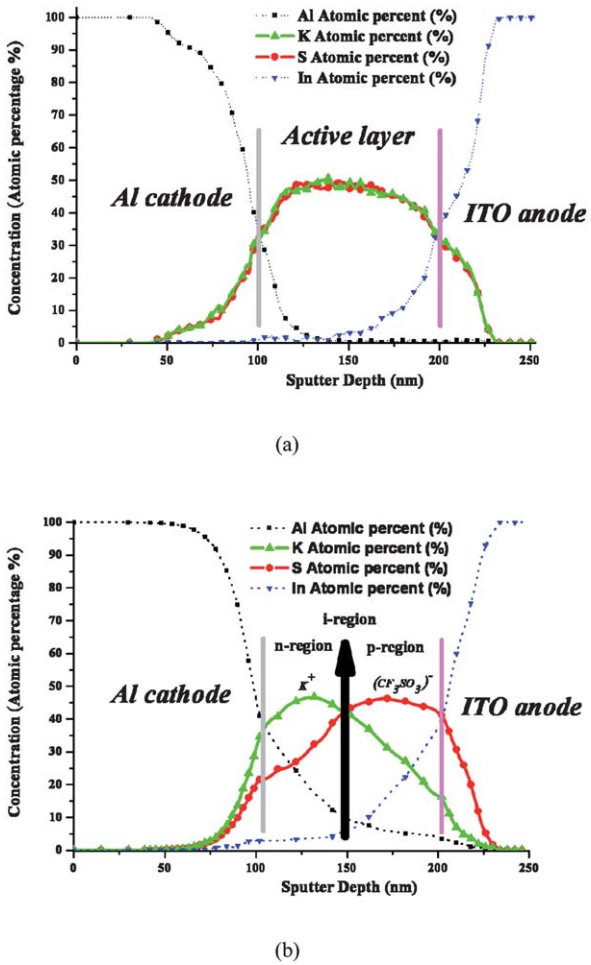


**Fig. 5** Auger depth profile of the MEH-PPV/PCBM devices, incorporating KOTf/PEO with and without a pre-bias of 3 V for 180 s, forming a p–i–n junction. (a) shows the Auger depth profile of the device without a pre-bias of 3 V for 180 s, and (b) shows the Auger depth profile of the device with a pre-bias of 3 V for 180 s, forming p–i–n junction.

$CF_3SO_3^-$ ion. In the Auger depth profile analysis, we identified the potassium (K) and sulfur (S) element energy peak intensities as indicators of the concentration of the positively charged ions ($K^+$) and negatively charged ions ($CF_3SO_3^-$), respectively, while collecting the energy peak signal of the Al element and In element intensity to represent the cathode (Al) and anode (ITO) concentrations. Fig. 5a showed the Auger depth profile of a device of MEH-PPV/PCBM incorporating the KOTf/PEO mixture: the concentration profile displayed is almost an equal distribution of the positively charged ions, $K^+$, and the negatively charged ions, $CF_3SO_3^-$, in the active layer, and therefore the active layer maintains electroneutrality for the doped device without applying a pre-bias voltage. In contrast, Fig. 5b presents an asymmetrical concentration profile for the KOTf/PEO doped MEH-PPV/PCBM device after applying a pre-bias: the positively charged ions shift to cathode (Al) and the negatively charged ions moved to anode (ITO). At the point where the concentration of the K and S elements are equivalent, it is defined as an intrinsic region. Moreover, we also observed that the p-type region width is larger than the n-type region and this phenomenon is consistent with previous reports.[18,19] The p-type region and the n-type region thicknesses can be deduced to be *ca.* 55 nm and *ca.* 40 nm, respectively, while the intrinsic region thickness is *ca.* 5 nm. In the Auger depth profile analysis, we used Ar gas to etch the sample and estimated the etched layer thickness during an etching period (10 s). The etched layer thickness for every etching period was about 5 nm. Fig. S3, ESI,†shows that less than 3% difference between the positive and negative ion distribution was found for one etching period. Therefore, we estimated that the i region thickness is about 5 nm. Hence, we directly confirm the formation of an asymmetrical p–i–n junction structure in the KOTf/PEO doped MEH-PPV/PCBM device after applied bias.

Fig. 6 displays the measured open-circuit voltages ($V_{oc}$), short-circuit current densities ($J_{sc}$), fill factors (FFs), and PCEs of the p–i–n MEH-PPV/PCBM photovoltaic devices incorporating metal triflate/PEO that had been pre-biased at various voltages for 180 s. Fig. 6a reveals that the value of $V_{oc}$ increased as the applied pre-bias voltages increased, presumably because the decrease in the voltage drops at the polymer–electrode interfaces, due to ohmic contacts induced by *in situ* electrochemical doping. Moreover, a common trend in Fig. 6a is that all of the devices pre-biased at 5 V and featuring metal triflate/PEO mixtures exhibited increased values of $V_{oc}$ that approached *ca.* 0.8 V, the ideal value of $V_{oc}$ for MEH-PPV/PCBM systems, as estimated from the energy level offset between the lowest unoccupied molecular orbital (LUMO) of PCBM and the highest occupied molecular orbital (HOMO) of MEH-PPV.[36–38] Because the accumulation of ions would be accelerated under a higher bias,[39] the resulting greater accumulation of ions would further reduce the potential drop in voltage, across the active layer and the cathode; the decreases in the voltage at the polymer–electrode interface would enhance the $V_{oc}$ of the device. Fig. 6b reveals that the changes in the $J_{sc}$ of the p–i–n photovoltaic devices occurred in two stages: initial increases upon increasing the pre-bias voltage, reaching a maximum at a pre-bias voltage of 3 V, and then decreases upon increasing the pre-bias voltage beyond that value. This phenomenon results from two counteracting factors: (i) the strength of the built-in electric field for exciton dissociation and (ii) the intrinsic layer thickness for generating majority excitons. In the first stage (pre-bias: 1–3 V), the improvement in

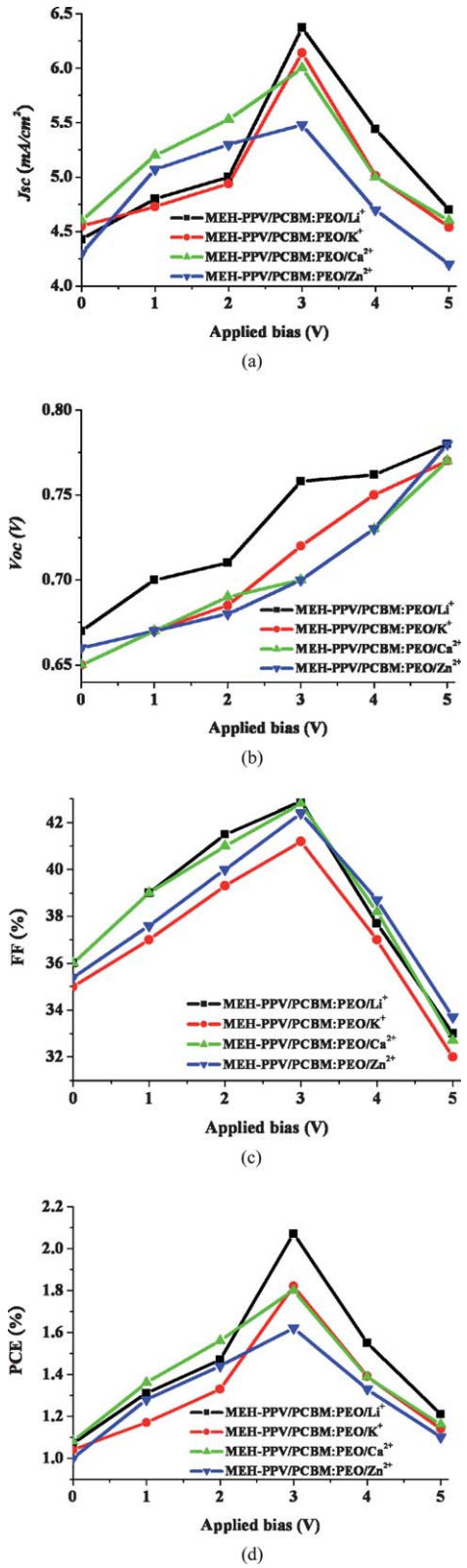


**Fig. 6** Plots of a) $V_{oc}$, b) $J_{sc}$, c) FF, and d) PCE of p–i–n photovoltaic devices prepared with LiOTf (square), KOTf (circle), $Ca(OTf)_2$ (triangle), and $Zn(OTf)_2$ (inverted triangle)/PEO mixtures pre-biased at various voltages for 180 s.

the exciton dissociation efficiency, due to the enhanced built-in electric field, was more dominant than the decrease in exciton generation, due to the thinner intrinsic layer, relative to that in the control device (pre-bias: 0 V), leading to a higher value of $J_{sc}$. When the devices experienced a higher pre-bias (4–5 V), the weighing factors were reversed: much fewer excitons were generated for a much thinner intrinsic layer, despite the larger built-in electric field, leading to a lower value of $J_{sc}$. Notably, the values of $J_{sc}$ for devices pre-biased at 3 V for 180 s increased significantly (up to >1.5 times) relative to those of devices that had not been subjected to pre-biasing. The pre-biased devices doped with metal triflate/PEO mixtures all exhibited much higher current densities than those of pure MEH-PPV/PCBM devices, due to the presence of p–i–n junctions induced by *in situ* electrochemical doping.[25,28,29] Among the devices, those doped with LiOTf/PEO featured the most significant enhancements in their current densities, presumably because the $Li^+$ cation, with its smallest ionic radius and lightest ionic mass, compared with those of $K^+$, $Ca^{2+}$ and $Zn^{2+}$, resulted in the development of well-formed p–i–n junctions within the limited pre-biasing time. Consequently, the improved exciton dissociation efficiency induced by the enhanced built-in electric field in the intrinsic layer increased the PCEs of the LiOTf/PEO-doped devices up to 2.07%. Fig. 6c presents the FFs of the p–i–n photovoltaic devices; we observe the same phenomenon as that for the values of $J_{sc}$, with an initial increase up to a maximum value at 3 V followed by a decrease upon increasing the pre-bias voltage. We attribute the initial increase in the FF to the decreased series resistance of the active layer after *in situ* electrochemical doping. Further increasing the pre-bias voltage resulted in a reduced thickness of the intrinsic layer, thereby facilitating doping-induced micro shorts[40] and, thereby lowering the shunt resistance of the active layer, leading to a lower FF. Fig. 6d presents a plot of the PCEs of the photovoltaic devices with respect to the pre-bias voltage; again, the trend follows those of the plots of $J_{sc}$ and FF. Among the devices doped with the LiOTf, KOTf, $Ca(OTf)_2$, and $Zn(OTf)_2$/PEO mixtures, the MEH-PPV/PCBM device incorporating the LiOTf/PEO mixture exhibited the highest PCE (2.07%), 40% greater than that of the control device (1.47%) that was fabricated under state of art conditions different to those of the doped devices. The MEH-PPV/PCBM device was fabricated under the same processing conditions as those of the doped devices and showed a PCE of only 1.26%. Again, we attribute this phenomenon to the $Li^+$ ions having the smallest ion radius and lightest ion mass; therefore, they would exhibit the best arrangement condition under the same electrical field, leading to well formed p–i–n structures. Our results indicate that *in situ* electrochemical doping is a promising technique for enhancing the PCEs of polymer photovoltaic devices.

*I–V* curves and EQE spectra for the MEH-PPV/PCBM photovoltaic devices prepared with and without LiOTf, KOTf, $Ca(OTf)_2$, and $Zn(OTf)_2$/PEO mixtures that had been pre-biased at 3 V for 180 s are shown in the ESI.†

Table 1 summarizes the photovoltaic characteristics of different devices which experienced a pre-bias of 3 V for 180 s. The enhancement in the EQE was consistent with the increased values of $J_{sc}$ which were induced by the improved exciton dissociation efficiency in the presence of an increased built-in electric field. Although the nature of the cation had a relatively

 

**Table 1** Photovoltaic characteristics of p–i–n MEH-PPV/PCBM photovoltaic devices prepared with and without metal triflate/PEO mixtures pre-biased at 3 V for 180 s

| Components of active layer | $V_{oc}$ (V) | $J_{sc}$ (mA cm$^{-2}$) | FF (%) | PCE (%) | Enhancement[a] (%) |
|---|---|---|---|---|---|
| MEH-PPV/PCBM[b] (1 : 4, w/w) | 0.72 | 4.67 | 42.8 | 1.47 | — |
| MEH-PPV/PCBM: PEO[b] | 0.79 | 4.07 | 44.1 | 1.43 | — |
| MEH-PPV/PCBM: LiOTf/PEO | 0.76 | 6.37 | 42.9 | 2.07 | 40 |
| MEH-PPV/PCBM: KOTf/PEO | 0.72 | 6.14 | 41.2 | 1.82 | 24 |
| MEH-PPV/PCBM: $Ca(OTf)_2$/PEO | 0.70 | 6.00 | 42.8 | 1.80 | 22 |
| MEH-PPV/PCBM: $Zn(OTf)_2$/PEO | 0.70 | 5.48 | 42.4 | 1.62 | 10 |

[a] Relative to the PCE of the pure MEH-PPV/PCBM (1 : 4, w/w) device. [b] The PCE of the MEH-PPV/PCBM and MEH-PPV/PCBM:PEO devices were fabricated under state of the art conditions. The PCE of the MEH-PPV/PCBM device was fabricated at the same conditions as the doped devices was 1.26%.

**Table 2** Endurance test[a] data of p–i–n MEH-PPV/PCBM photovoltaic devices prepared with and without LiOTf/PEO mixtures pre-biased at 3 V for 180 s

| Components of active layer (endurance test time) | Normalized $V_{oc}$ (%) | Normalized $J_{sc}$ (%) | Normalized FF (%) | Normalized PCE (%) |
|---|---|---|---|---|
| MEH-PPV:PCBM[b] (0 h) | 100 | 100 | 100 | 100 |
| MEH-PPV:PCBM (5 h) | ***83.14*** | ***92.53*** | ***89.85*** | ***69.12*** |
| MEH-PPV/PCBM: LiOTf/PEO (0 h) | 100 | 100 | 100 | 100 |
| MEH-PPV/PCBM: LiOTf/PEO (5 h) | ***77.14*** | ***85.08*** | ***83.14*** | ***54.56*** |
| Re-biased[c] MEH-PPV/PCBM: LiOTf/PEO (5 h) | ***85.22*** | ***94.3*** | ***84.72*** | ***68.48*** |

[a] Photovoltaic data was collected under simulated AM 1.5G solar radiation (100 mW cm$^{-2}$) in a $N_2$-filled glove box for 5 h of continuous operation. [b] When the MEH-PPV/PCBM devices were also subjected to pre-biasing at 3 V for 180 s, the device performance was unaffected. [c] The device was re-biased at 3 V for 180 s after 5 h of continuous operation.

slight effect on the values of $V_{oc}$ for the pre-biased metal triflate/PEO–incorporated MEH-PPV/PCBM photovoltaic devices, it had a large effect on the values of $J_{sc}$.

Our MEH-PPV/PCBM devices doped with metal triflate/PEO mixtures exhibited shorter response times (180 s), relative to those (1 to 6 h) of ionic liquid–doped PPV derivatives,[42] for forming their p–i–n junctions under the applied pre-bias voltages. The anions and cations, however, would relax back when the applied bias voltage was removed.[41–44] To examine the stability of the p–i–n junction structures within the LiOTF/PEO–doped MEH-PPV/PCBM devices that had experienced pre-biasing at 3 V for 180 s, we performed endurance tests by exposing the devices under simulated AM 1.5G solar radiation at an intensity of 100 mW cm$^{-2}$ in a $N_2$ glove box for 5 h of continuous operation.

Table 2 lists the percentage decreases in the values of $V_{oc}$, $J_{sc}$, FF, and PCE of the devices prepared with and without LiOTf/PEO mixtures after 5 h continuous illumination. The PCE of the LiOTf/PEO–doped MEH-PPV/PCBM device decreased to *ca.* 55% of its initial value, while that of the MEH-PPV/PCBM device decreased to *ca.* 70% to its initial value. With subsequent re-biasing at 3 V for 180 s, the PCE of the LiOTf/PEO–doped device recovered to *ca.* 68% of its initial value. We observed similar phenomena for the values of $V_{oc}$, $J_{sc}$, and FF for the re-biased LiOTf/PEO–doped devices (Table 2). Therefore, it appears that the larger decreases in $V_{oc}$, $J_{sc}$, FF, and PCE for the LiOTf/PEO–doped devices, relative to those of the corresponding pure MEH-PPV/PCBM devices, after 5 h of continuous operation can be attributed to the relaxation of the p–i–n junctions, a phenomenon commonly observed in LECs.[26,27] Improvements of the relaxation times of p–i–n structure within devices have been demonstrated using "frozen" p–i–n junctions[42,45,46] and "covalent bonding."[47]

## Conclusions

We have applied a pre-bias to metal triflate/PEO–incorporated MEH-PPV/PCBM photovoltaic devices to form p–i–n junctions in the active layers. AC capacitance analyses of the device indicated the presence of p–i–n junctions and revealed that the intrinsic layer was thinner when formed under higher pre-bias voltages. Auger depth profile analysis revealed the distribution of positive and negative ions and confirmed the formation of an asymmetrical p–i–n junction structure in a thin layer of *ca.* 100 nm. AFM imaging revealed that addition of metal triflate/PEO to MEH-PPV/PCBM improved the morphology of the composite films. Among the devices doped with the metal triflate/PEO mixtures, the MEH-PPV/PCBM device incorporating the LiOTf/PEO mixture exhibited the highest PCE, an increase of 40% relative to that of the control device. Thus, the formation of p–i–n junctions through *in situ* electrochemical doping is a promising approach toward enhancing the performance of polymer photovoltaic devices.

## References

1 Changduk Yang, Jae Kwan Lee, Alan J. Heeger and Fred Wudl, *J. Mater. Chem.*, 2009, **19**, 5416.
2 M. Lenes, F. B. Kooistra, J. C. Hummelen, I. V. Severen, L. Lutsen, D. Vanderzande, T. J. Cleij and P. W. M. Blom, *J. Appl. Phys.*, 2008, **104**, 114517.

3 T. Kirchartz, J. Mattheis and U. Rau, *Phys. Rev. B: Condens. Matter Mater. Phys.*, 2008, **78**, 235320.
4 J. Nelson, J. J. Kwiatkowski, J. Kirkpartrick and J. M. Frost, *Acc. Chem. Res.*, 2009, **42**, 1768.
5 C. Groves, J. C. Blakesley and N. C. Greenham, *Nano Lett.*, 2010, **10**, 1063.
6 M. C. Scharber, D. Mühlbacher, M. Koppe, P. Denk, C. Waldauf, A. J. Heeger and C. J. Brabec, *Adv. Mater.*, 2006, **18**, 789.
7 H. L. Yip, S. K. Hau, N. S. Baek, H. Ma and A. K. Y. Jen, *Adv. Mater.*, 2008, **20**, 2376.
8 V. D. Mihailetchi, P. W. M. Blom, J. C. Hummelen and M. T. Rispens, *J. Appl. Phys.*, 2003, **94**, 6849.
9 L. M. Chen, Z. Xu, Z. Hong and Y. Yang, *J. Mater. Chem.*, 2010, **20**, 2575.
10 K. StevenHau, Hin-Lap Yip, Orb Acton, Nam Seob Baek, Hong Ma and Alex K.-Y. Jen, *J. Mater. Chem.*, 2008, **18**, 5113.
11 H. S. Wang, L. H. Lin, S. Y. Chen, Y. L. Wang and K. H. Wei, *Nanotechnology*, 2009, **20**, 075201.
12 P. Yu, C. H. Chang, M. S. Su, M. H. Hsu and K. H. Wei, *Appl. Phys. Lett.*, 2010, **96**, 153307.
13 M. Y. Chiu, U. S. Jeng, C. H. Su, K. S. Liang and K. H. Wei, *Adv. Mater.*, 2008, **20**, 2573.
14 M. Y. Chiu, U. S. Jeng, M. S. Su and K. H. Wei, *Macromolecules*, 2010, **43**, 428.
15 A. Liu, S. Zhao, S. B. Rim, J. Wu, M. Konemann, P. Erk and P. Peumans, *Adv. Mater.*, 2008, **20**, 1065.
16 B. A. Greeg, *Soft Matter*, 2009, **5**, 2985.
17 J. M. Leger, S. A. Carter and B. Ruhstaller, *J. Appl. Phys.*, 2005, **98**, 124907.
18 L. S. C. Pingree, D. B. Rodovsky, D. C. Coffey, G. P. Bartholomew and D. S. Ginger, *J. Am. Chem. Soc.*, 2007, **129**, 15903.
19 Juhyun Park, Corey V. Hoven, Renqiang Yang, Namsung Cho, Hongbin Wu, Thuc-Quyen Nguyen and Guillermo C. Bazan, *J. Mater. Chem.*, 2009, **19**, 211.
20 F. Maddalena, E. J. Meijer, K. Asadi, D. M. de Leeuw and P. W. M. Blom, *Appl. Phys. Lett.*, 2010, **97**, 043302.
21 J. Drechsel, B. Männig, F. Kozlowski, D. Gebeyehu, A. Werner, M. Koch, K. Leo and M. Pfeiffer, *Thin Solid Films*, 2004, **451**, 515.
22 B. Männig, J. Drechsel, D. Gebeyehu, P. Simon, F. Kozlowski, A. Werner, F. Li, S. Grundmann, S. Sonntag, M. Koch, K. Leo, M. Pfeiffer, H. Hoppe, D. Meissner, N. S. Sariciftci, I. Reidel, V. Dyakonov and J. Parisi, *Appl. Phys. A: Mater. Sci. Process.*, 2004, **79**, 1.
23 C. Falkenberg, C. Uhrich, S. Olthof, B. Maennig, M. K. Riede and K. Leo, *J. Appl. Phys.*, 2008, **104**, 034506.
24 W. Y. Gao and A. Kahn, *Org. Electron.*, 2002, **3**, 53.
25 J. Gao, G. Yu and A. J. Heeger, *Adv. Mater.*, 1998, **10**, 692.
26 Q. Pei, G. Yu, C. Zhang, Y. Yang and A. J. Heeger, *Science*, 1995, **269**, 1086.
27 Q. Pei, Y. Yang, G. Yu, C. Zhang and A. J. Heeger, *J. Am. Chem. Soc.*, 1996, **118**, 3922.
28 J. M. Leger, D. G. Patel, D. B. Rodovsky and G. P. Bartholomew, *Adv. Funct. Mater.*, 2008, **18**, 1212.
29 Z. Yu, M. Sun and Q. Pei, *J. Phys. Chem. B*, 2009, **113**, 8481.
30 V. Shrotriya, G. Li, Y. Yao, T. Moriarty, K. Emery and Y. Yang, *Adv. Funct. Mater.*, 2006, **16**, 2016.
31 Y. T. Chang, S. L. Hsu, M. H. Su and K. H. Wei, *Adv. Mater.*, 2009, **21**, 2093.
32 K. Emery, *Sol. Cells*, 1986, **18**, 301.
33 F. C. Chen, Q. Xu and Y. Yang, *Appl. Phys. Lett.*, 2004, **84**, 3181.
34 Y. Li, J. Gao, G. Yu, Y. Cao and A. J. Heeger, *Chem. Phys. Lett.*, 1998, **287**, 83.
35 G. Yu, Y. Cao, C. Zhang, Y. Li, J. Gao and A. J. Heeger, *Appl. Phys. Lett.*, 1998, **73**, 111.
36 Fred Wudl, *J. Mater. Chem.*, 2002, **12**, 1959.
37 B. C. Thompson and J. M. J. Frechet, *Angew. Chem., Int. Ed.*, 2008, **47**, 58.
38 L. J. A. Koster, E. C. P. Smits, V. D. Mihailetchi and P. W. M. Blom, *Phys. Rev. B: Condens. Matter Mater. Phys.*, 2005, **72**, 085205.
39 P. Matyba, K. Maturova, M. Kemerink, N. D. Robinson and L. Edman, *Nat. Mater.*, 2009, **8**, 672.
40 J. H. Shin, S. Xiao and L. Edman, *Adv. Funct. Mater.*, 2006, **16**, 949.
41 L. Edman, M. Pauchard, D. Moses and A. J. Heeger, *J. Appl. Phys.*, 2004, **95**, 4357.
42 Y. Shao, G. C. Bazan and A. J. Heeger, *Adv. Mater.*, 2007, **19**, 365.
43 C. Hoven, R. Yang, A. Garcia, A. J. Heeger, T. Q. Nguyen and G. C. Bazan, *J. Am. Chem. Soc.*, 2007, **129**, 10976.
44 F. P. Wenzl, P. Pachler, C. Suess, A. Haase, E. J. W. List, P. Poelt, D. Somitsch, P. Knoll, U. Scherf and G. Leising, *Adv. Funct. Mater.*, 2004, **14**, 441.
45 J. Gao, G. Yu and A. J. Heeger, *Appl. Phys. Lett.*, 1997, **71**, 1293.
46 G. Yu, Y. Cao, M. Anderson, J. Gao and A. J. Heeger, *Adv. Mater.*, 1998, **10**, 385.
47 C. V. Hoven, H. Wang, M. Elbing, L. Garner, D. Winkelhaus and G. C. Bazan, *Nat. Mater.*, 2010, **9**, 249.


 